One-Pot Heterointerfacial Metamorphosis for Synthesis and Control of Widely Varying Heterostructured Nanoparticles

Mouhong Lin,[∥] Jian Wang,[∥] Gyeong-Hwan Kim,[∥] Jianan Liu, Limin Pan, Yeonhee Lee, Jeong-Wook Oh, Yoonjae Jung, Sungjae Seo, Youngju Son, Jongwoo Lim, Jungwon Park, Taeghwan Hyeon, and Jwa-Min Nam*

Cite This: https://dx.doi.org/10.1021/jacs.0c11557

Read Online

ACCESS | Metrics & More | Article Recommendations | SI Supporting Information

ABSTRACT: Despite remarkable facileness and potential in forming a wide variety of heterostructured nanoparticles with extraordinary compositional and structural complexity, one-pot synthesis of multicomponent heterostructures is largely limited by the lack of fundamental mechanistic understanding, designing principles, and well-established, generally applicable chemical methods. Herein, we developed a one-pot heterointerfacial metamorphosis (1HIM) method that allows heterointerfaces inside a particle to undergo multiple equilibrium stages to form a variety of highly crystalline heterostructured nanoparticles at a relatively low temperature (<100 °C). As proof-of-concept experiments, it was shown that widely different single-crystalline semiconductor−metal anisotropic nanoparticles with synergistic chemical, spectroscopic, and band-gap-engineering properties, including a series of metal−semiconductor nanoframes with high structural and compositional tunability, can be formed by using the 1HIM approach. 1HIM offers a new paradigm to synthesize previously unobtainable or poorly controllable heterostructures with unique or synergistic properties and functions.
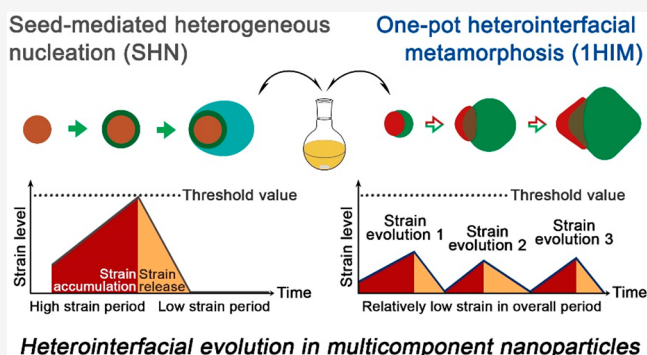
1. INTRODUCTION

Synthesis of heterostructured nanoparticles (hetero-NPs) with precisely controlled geometries, configurations, and crystal structures of the multiple components is of paramount importance and can provide new directions and opportunities in nanoscience and materials research;[1−3] however, realizing this for a wide variety of different hetero-NPs is highly challenging. Particularly, the controlled growth of hetero-NPs that contain single-crystalline semiconductor domains has been desired for the in-depth exploration of semiconductor physics and their interactions with other components.[4−7] In 2010, the synthesis of isotropic metal−semiconductor core−shell nano-structures with single-crystalline semiconductor shells was reported, and it was shown that the heterointerface between largely mismatched seed and shell can be reconstructed in a nonepitaxial manner by introducing an amorphous-to-crystal-line transition process.[7] Recently, semiconductor-involved anisotropic heterostructures have found tremendous advantages over their core−shell counterparts for enhanced charge-transfer dynamics,[8,9] engineered electronic band gap,[10] tunable junction physics,[11] and various new optoelectronic proper-ties.[12] However, the mechanistic understanding, as well as the controllable and tunable synthetic methods for anisotropic hetero-NPs, especially with semiconductor−metal anisotropic NPs (SMAPs), is still lacking.

Seed-mediated heterogeneous nucleation (SHN) has been the widely adopted method in the chemical synthesis of hetero-NPs. Typically, a secondary material can be grown on seed particles by wet-chemistry approaches, having been demonstrated with a broad range of colloidal heterostructures with semiconductors,[7−11] metals,[7−9,11,13,14] and oxides.[15−17] By separating the seed nucleation step from the heterointerface formation step, the SHN method can independently control the morphology of the seed domain and the size and shape of the shell domain to some degree. However, the high lattice strain induced by the heterointerface often leads to a locally overstressed shell,[18] which largely inhibits the formation of a single-crystalline domain[7] and can result in poor control over the geometry and crystal structure of the hetero-NPs. There is also a clear limitation in forming a wide range of heterostructured nanoparticles, particularly controlling hetero-interfaces inside a particle with SHN methods.
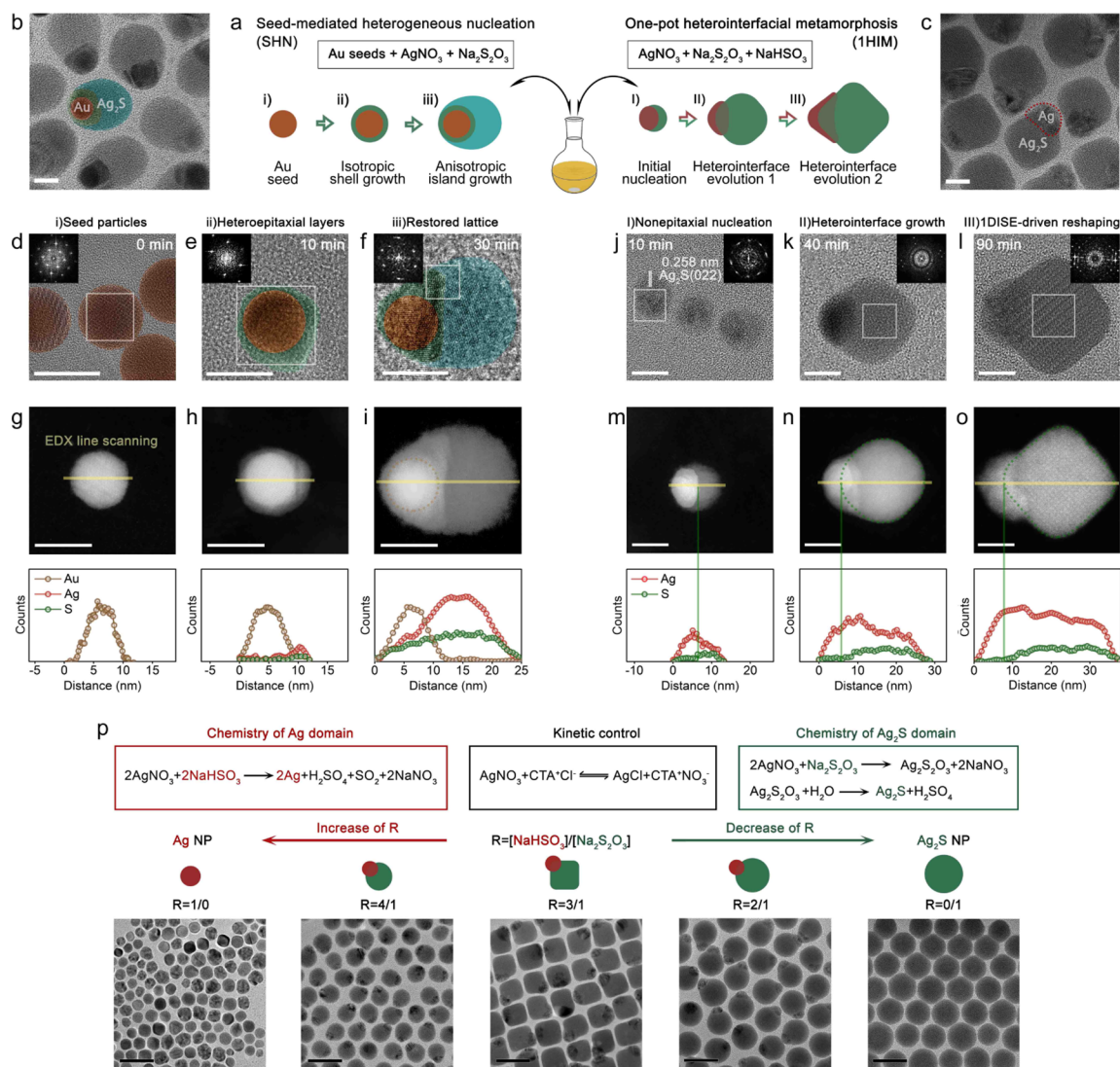
Figure 1. Heterointerface evolution behaviors in multicomponent nanoparticles. (a) Schematic comparison of the typical seed-mediated heterogeneous nucleation (SHN) method with the one-pot heterointerfacial metamorphosis (1HIM) method in the synthesis of metal–silver sulfide heterostructures. Transmission electron microscope (TEM) images of SHN-prepared heterostructures (b) and 1HIM-synthesized heterostructures (c). High-magnification images of various growth stages of SHN products (d–f) and 1HIM (j–l) products. Insets show the corresponding fast Fourier transform (FFT) patterns of the selected areas. HAADF images and EDX line scanning profiles showing the heterointerfaces and corresponding elemental distributions of various growth stages of SHN products (g–i) and 1HIM products (m–o). (p) Optimization strategies of the 1HIM. Briefly, through the chemical equilibrium between $AgNO_3$ and $AgCl$ (the chemical equation in the black box), the Ag^+ concentration can be maintained at a relatively low level, and the growth kinetics of Ag and Ag_2S can be independently controlled through two chemical reactions: reduction of the Ag domain (the chemical equation in the red box) and formation of the Ag_2S domain (the chemical equation in the green box). Therefore, the reaction kinetics of each domain and the resulting nanostructures can be finely tuned via the concentration ratio (R) of $NaHSO_3$ (the reductant for the Ag domain) to $Na_2S_2O_3$ (sulfur precursor for the Ag_2S domain) ($R = [NaHSO_3]/[Na_2S_2O_3]$). Scale bars are 10 nm (b–o) and 100 nm (p), respectively.

Here, we report the one-pot heterointerfacial metamorphosis (1HIM) method for the high-yield synthesis of a wide variety of SMAPs with diverse heterointerfaces in aqueous solution. Due to the newly emerging strain evolution behavior, the 1HIM method demonstrated the growth of heterostructures with a single-crystalline semiconductor domain in an anisotropic manner. Moreover, the new heterostructure-designing logic and structural evolution pattern present unprecedented synthetic tunability over the shape (ranging from cube to ellipsoid, bipyramid, rod, parallelepiped, and octahedron), crystal structure, and secondary structure. Importantly, widely varying heterostructured nanoframes with fine compositional and structural tunability can be

obtained using the 1HIM method. It was also found that synergistic properties can be obtained by forming these heterostructures; these includes largely improved chemical stability, stronger signals in surface-enhanced Raman scattering (SERS) of the metal domain by forming metal–semiconductor heterostructures, and unique band gap tunability in metal–semiconductor hetero-NPs due to the highly engineerable primary and secondary structures in these heterostructures.

2. EXPERIMENTAL SECTION

2.1. Synthesis of Colloidal SMAPs. In a typical synthesis of cubic SMAPs (cSMAPs), $Na_2S_2O_3$ (0.1 M, 60 μL), $NaHSO_3$ (0.1 M, 180 μL), and $AgNO_3$ (0.1 M, 150 μL) were added into a well-

dissolved solution of cetyltrimethylammonium chloride (CTAC, 10 mL) with stirring (200 rpm) at 95 °C. The solution color gradually changed from transparent to yellowish brown. The reaction was allowed to continue at 95 °C for 90 min before washing with 10 mM ammonia solution (once) and 1 mM CTAC solution (twice) by centrifugation at 12 000 rpm. The final products were redispersed and stored in 1 mL of 1 mM CTAC solution before use. The size of the cSMAPs was controlled by the concentration of CTAC, which was varied from 80 to 100, 140, 160, and 200 mM for cSMAP21, cSMAP26, cSMAP38, cSMAP50, and cSMAP65, respectively.

2.2. Synthesis of Structure-Engineered SMAPs. First, a 4-MBA solution (1 mM) was freshly prepared in ethanol and fully dissolved by sonication. In a typical experiment, a certain amount of 4-MBA solution was mixed with CTAC (0.5 mL) with stirring, which was then combined with a mixture of CTAC (0.5 mL), $Na_2S_2O_3$ (0.1 M, 6 μL), $NaHSO_3$ (0.1 M, 18 μL), and $AgNO_3$ (0.1 M, 15 μL). The resulting mixture was heated at 95 °C for 120 min before washing with 10 mM ammonia solution (once) and 1 mM CTAC solution (twice) by centrifugation. The final products were redispersed and stored in 1 mL of 1 mM CTAC solution before use. The geometry of the Ag_2S domains were tuned by the amount of 4-MBA, which was varied from 4 to 6, 9, 11, and 15 μL for eSMAP, bSMAP, rSMAP, pSMAP, and oSMAP, repectively. The concentration of CTAC was tuned to control the growth kinetics for each structure and optimized at 200, 160, 100, 100, and 100 mM for eSMAP, bSMAP, rSMAP, pSMAP, and oSMAP, respectively.

2.3. Synthesis of Metal−Semiconductor Nanoframes (MSFs). First, an aqueous solution of K_2PtCl_4 (5 mM) was dissolved by sonication and remained overnight before use. In a typical experiment, a certain amount of K_2PtCl_4 solution (5 mM, 40 μL) was mixed with CTAC (80 mM, 0.5 mL), $Na_2S_2O_3$ (0.1 M, 6 μL), and $NaHSO_3$ (0.1 M, 18 μL) with stirring, which was then combined with a mixture of CTAC (80 mM, 0.5 mL) and $AgNO_3$ (0.1 M, 15 μL). The resulting mixture was heated at 95 °C for 120 min before washing with 10 mM ammonia solution (once) and 1 mM CTAC solution (twice) by centrifugation (6000 rpm, 10 min). The final products were redispersed and stored in 100 μL of 1 mM CTAC solution. The structure of the nanoframes was tuned by the concentration ratio of K_2PtCl_4 to $NaHSO_3$, ranging over 35/15, 38/16, 40/18, and 42/20 for MSF I, MSF II, MSF III, and MSF IV, respectively.

2.4. Synchrotron Radiation X-ray Scattering (XRS) Measurements. XRS spectra were recorded in a liquid base, ex situ manner on an MAR345 image plate with an incident wavelength of 1.0332 Å (12 keV) from a synchrotron X-ray source at the Pohang Accelerator Laboratory (beamline 3D, Pohang, Korea). The cell used for measurements was sealed by Kapton tape with an aperture of 3 mm for a beam path. The 2θ data were obtained by circularly integrating the pixels on a flat image plate detector, which is calibrated with the standard reference LaB_6 powder.

3. RESULTS AND DISCUSSION

To understand the fundamental growth behavior of hetero-NPs, a side-by-side comparison was performed between the SHN and 1HIM methods in terms of the lattice formation process, heterointerface evolution behavior, and strain evolution pattern using a monoclinic α-silver sulfide (Ag_2S)/face-centered cubic (fcc) metal heterostructure as a model system (Figure 1a). We compared two anisotropic hetero-structures, Au/Ag_2S hetero-NP (Figure 1b) and Ag−Ag_2S hetero-NP (Figure 1c), formed by the SHN and 1HIM methods, respectively. As shown in Figure 1a, a typical SHN process involves the synthesis of nanoparticle seeds (stage i, Figure 1d) and the subsequent heteronucleation of shell material on the seeds. Driven by thermodynamics, hetero-epitaxial growth was favored at the initial stage of shell nucleation (stage ii, Figure 1e), known as a pseudomorphic shell.[18] After the growth of several atomic layers, the formation of shell domains shifted from isotropic growth to anisotropic

island growth (stage iii, Figure 1f). Meanwhile, the structure of the newly formed shell started to restore its thermodynamically favored lattice through atom dislocations, resulting in the polycrystalline shell (Figure 1f). The shape of the Au seed (Figure 1g), the boundary of Au/Ag_2S (Figure 1h), and the polycrystalline Ag_2S shell (Figure 1i) were clearly evidenced by high-angle annular dark-field (HAADF) images and energy dispersive X-ray spectroscopy (EDX) line scanning.

In contrast, the 1HIM method, which throws all metal and semiconductor precursors and reagents into a solution together, experiences evolutionary expansions of heterointerfaces and continuous reshaping. Janus heteroseeds composed of a multitwinned Ag domain and a single-crystalline Ag_2S domain were nucleated within 20 min (stage I, Figure 1j). After 40 min of reaction (stage II, Figure 1k), the shape of the Ag_2S domain gradually evolved into a more isotropic round-cornered cube, while the Ag domain grew into a highly anisotropic polycrystalline structure. After 90 min of reaction (stage III, Figure 1l), the size difference between Ag_2S and Ag domains increased as the cubic shape of the Ag_2S domain further sharpened, which was referred to as cubic SMAPs (cSMAPs) [Figure S1, Supporting Information (SI)]. The exposure of the Ag surface is shown in TEM images (Figure 1g−i), EDX results (Figure S2, SI), and X-ray photoelectron spectroscopy data (XPS, Figure S3, SI), indicating formation of a Janus structure with a clear subparticle boundary, which was not observed with the hetero-NPs synthesized with the SHN method. The evolution of heterointerfaces was clearly observed by HAADF images and EDX line scanning (Figure 1m−o). Initiated from an ellipsoidal shape of the Ag domain due to stronger metal−metal bonds, the shape of the heterointerface transformed from a Ag convex-shaped interface (Figure 1m) to a Ag concave-shaped interface (Figure 1n,o) as the size of the Ag_2S domain increased. The boundaries of the heterointerface were further analyzed by the elemental distribution of sulfur, as indicated by EDX line scanning, which clearly showed the evolutionary expansion of heterointerfaces in stages II and III along with reshaping of the Ag_2S domain (Figure 1n,o). Such a controlled anisotropic growth and evolutionary heterointerface should be attributed to the well-optimized chemical environment in the 1HIM approach. As shown in Figure 1p, we designed multiple chemical equilibria and domain reactions to create chemical environments that allow independent control of surface chemistries and growth kinetics of different components inside hetero-NPs. It should be noted that cetyltrimethylammonium chloride (CTA^+Cl^- or CTAC) plays a key role and is used as a surface ligand to manipulate the reaction kinetics and the surface energies of multiple components simultaneously. The growth kinetics of the domains inside hetero-NPs can be manipulated by the R value that is associated with the two independent chemistries. In the extreme cases with $R = 1/0$ or $R = 0/1$, it was confirmed that only single-component particles were formed. By decreasing R values (from 2/1 to 4/1), the size of the Ag domain gradually decreased while that of the Ag_2S domain gradually increased. During this process, different atom deposition rates in two components can result in different heterointerface structures and strain equilibrium stages, such as the cubic geometry at $R = 3/1$. In this way, the 1HIM strategy provides diverse and powerful ways to explore multiple equilibrium stages and unexpected heterointerfaced nanostructures.
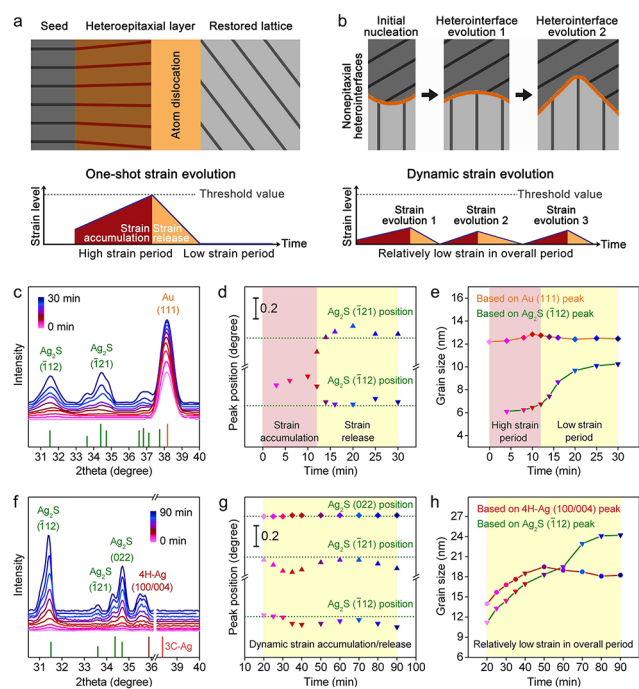
Figure 2. Heterointerfacial strain evolution behaviors. Schematic illustrations of the one-shot strain evolution process in the SHN method (a) and the heterointerfacial metamorphosis process in the 1HIM method (b). Liquid-based, ex situ synchrotron radiation X-ray scattering (XRS) patterns monitoring the growth solutions of the SHN (c) and 1HIM (f) approaches, as a function of reaction time. Recorded Ag_2S major peak positions in the XRS patterns corresponding to the SHN (d) and 1HIM (g) approaches. Size evolution of the metal and semiconductor domains calculated by the Debye−Scherrer equation from XRS patterns corresponding to the SHN (e) and 1HIM (h) approaches.

To investigate the 1HIM mechanism, we then employed the synchrotron radiation X-ray scattering (XRS) measurement to monitor the temporal evolutions of the crystal structure, lattice strain, and domain size of heterostructures in liquid form (Figure 2). As demonstrated elsewhere[18] and herein, the SHN method shows a one-shot strain evolution behavior, where lattice strain accumulates with heterointerface expansion to reach the threshold value, followed by atom dislocation to release strain (Figure 2a). The XRS results show that the Ag_2S peaks appeared within a few minutes of growth (Figure 2c). The strain level, which is proportional to the maximum peak offset from the reference peak position, can be also estimated by XRS (Figure 2d,g), and the grain size of each domain can be calculated by the Debye−Scherrer equation (Figure 2e,h). As shown in Figure 2d, the ($\bar{1}12$) peak of Ag_2S exhibited a large peak shift at the early stage (<10 min), which then sharply dropped to a normal level within the next 5 min. Such results are consistent with the HRTEM observations that hetero-epitaxial growth cannot be maintained after stage i (Figure 1e), thus restoring the thermodynamically favored lattice to form a polycrystalline shell. Meanwhile, the growth kinetics of both domains was also affected by strain evolution. As shown in Figure 2e, the size of the Ag_2S domain quickly increased during the strain release period, while the size evolution of the Au domain can be attributed to lattice expansion during the high-strain period. In contrast, the 1HIM method results in a dynamic strain evolution pattern with multiple equilibrium stages (Figure 2b). Starting from a nonepitaxial initial

nucleation, the dynamic expansion of heterointerface experienced multiple strain-equilibrium-driven heterointerfaces without reaching a threshold value, allowing the heterointerface-expansion-accumulated strain to be dynamically released through evolutionary heterointerfaces (Figure 1m−o) and strain-releasing structural transitions in domain structures. As shown in Figure 2f, the strongest and second strongest XRS peaks of Ag_2S in the cSMAP are found to be ($\bar{1}12$) and (022), respectively, while the strongest peak for bulk α-Ag_2S (PDF #14-0072) is ($\bar{1}21$). Meanwhile, the peak positions of ($\bar{1}12$) and ($\bar{1}21$) in the cSMAP were slightly shifted toward a higher angle (Figure 2g), suggesting an adjustment of crystal structure. Moreover, the position of the (022) peak experienced minor changes during the growth (Figure 2g), while those of ($\bar{1}12$) and ($\bar{1}21$) shift back and forth around the standard value. This suggests that (022) may be the strain-free growth direction, and the adjustment of the ($\bar{1}12$) and ($\bar{1}21$) peaks may be subjected to strain-releasing structural transitions. Both 4H-Ag (major phase) and 3C-Ag (minor phase) were observed under TEM (Figure S2d, SI), but only the diffraction peak of 4H-Ag was resolved in the XRS spectra. This can be attributed to the following reasons: (a) The strongest peak of 3C-Ag is partially overlapped with a strong peak of α-Ag_2S (($\bar{1}03$), 37.7°). Interfaced with α-Ag_2S, Ag is likely to endure lattice expansion, leading to the shift of the 3C-Ag peak (⟨111⟩, 38.1°) toward a lower angle and further overlapping with α-Ag_2S (($\bar{1}03$), 37.7°). (b) The high strain in the Ag body promotes the formation of the polycrystalline structure, which decreases the grain size of Ag and thus greatly broadens the 3C-Ag peaks. (c) The Ag size is much smaller than that of α-Ag_2S, which further decreases the resolution of the spectra. Moreover, the peak position of 4H-Ag remained over 1° away from the standard value and was finally split into two unresolved peaks (Figure 2f), indicating that the Ag domain endured more structural transitions to release lattice strain. Meanwhile, the size evolution of the domains also suggests the existence of structural reorganization. The Ag and Ag_2S domains have similar growth rates at the beginning (<50 min of reaction time), followed by rapid growth of the Ag_2S domain while the Ag domain slightly decreased, which may be a result of simultaneous evolution of the heterointerface and domain structure (Figure 2h). These results together with the TEM observations suggest that the 1HIM method provides a strain/structural evolution pattern and growth mechanism distinct from those of the SHN method, providing a new mechanism with a chance to form previously unobtainable hetero-NPs with unique heterointerfaces.

In fact, the underlying logic in hetero-NPs synthesis is vastly different from the thermodynamic and kinetic controls in single-component systems,[19,20] which explains the failure of directly "borrowing" fundamental understandings and synthetic tools in the synthesis of single-component structures for hetero-NPs. On the basis of previous studies and our results, we believe that the underlying logic in engineering hetero-NPs should be mainly based on precise strain management. As soon as heterointerfaces are formed, the arrangement and electronic structure of atoms are greatly distorted, which offers a new window for generating and tuning "new structures" or "new properties".[21] This tendency is, however, being also adjusted by thermodynamics, in the form of lattice strain, to restore their thermodynamically favored structure. If the strain level is well-managed, such a tendency of strain releasing can be employed to drive the formation of new structures. Taking
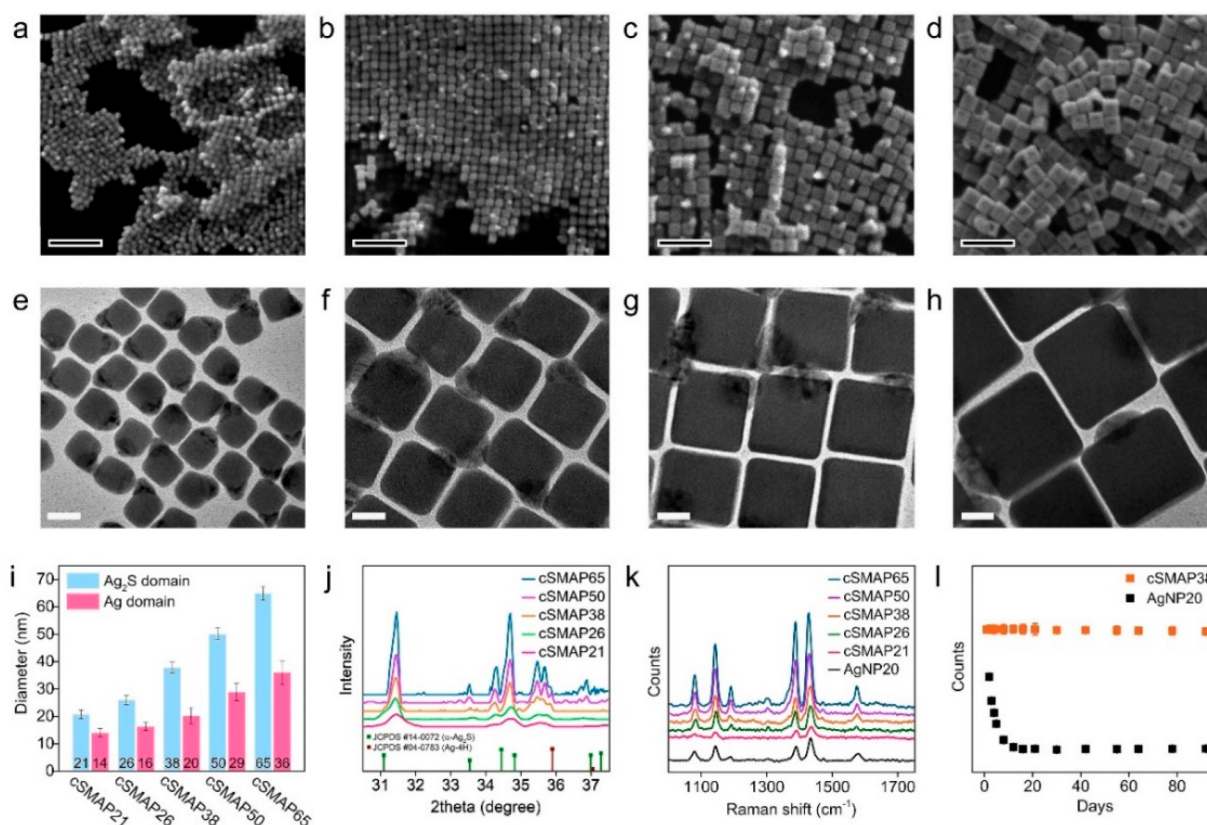
Figure 3. Structural evolution and new properties. SEM (a−d) and TEM images (e−h) of cSMAPs with various sizes. (i) Statistical analysis of domain diameters in various cSMAPs, which are referred to as cSMAPx with x representing the corresponding size of the Ag_2S domain. (j) Synchrotron radiation X-ray scattering (XRS) patterns of various cSMAPs. (k) Surface-enhanced Raman scattering (SERS) patterns of various cSMAPs and a 20 nm Ag NP (AgNP20) with a fixed particle concentration of 10 pM using 4-aminothiophenol (ATP) as the Raman dye at a laser wavelength of 514 nm. (l) SERS intensities at 1435 cm^{-1} that were recorded from cSMAP38 and AgNP20. Error bars came from three parallel measurements. Scale bars are 200 nm (a−d) and 20 nm (e−h).

semiconductors as an example, the surface energy difference between multiple facets of semiconductors is usually smaller comparing to that in metals,[22] which does not favor a facet-selective growth. Moreover, the covalent/ionic bonds in semiconductors are much more rigid than metallic bonds, possessing a higher energy barrier for atom dislocation. Therefore, if we take advantage of the semiconductor/metal heterointerface through the 1HIM strategy, the release of lattice strain should prefer the relatively low-energy-barrier pathways, such as heterointerface transformation and atom dislocations in metallic domains, thus promoting the formation of single-crystalline semiconductor domains with a minor structural transition.

The surface-ligand-based engineering of metal nanocubes is typically explained by the facet-selective preferential growth on symmetric seeds.[19,20] However, the presence of a heterointerface in hetero-NPs breaks the symmetries in both surface (facet) energies and facet-growth kinetics, which suggests that the shape formation mechanism of cubic hetero-NPs is mainly strain-related rather than facet-related. In our case, the cubic shape of the Ag_2S domain was gradually formed during the expansion of the heterointerface (Figure 1j−l) and further sharpened as particle size increased (Figure 3a−i), while the XRS patterns (Figures 2f and 3j) exhibited consistent enhancement and inhibition of specific peaks in all cases, indicating that there is a continuous driving force. Moreover, a concave cubic structure was clearly observed by the scanning electron microscope (SEM) images in Figure 3a−d, which

further supports a mechanism of strain-releasing structural transitions. Importantly, these cSMAPs showed strong surface-enhanced Raman scattering (SERS) activity and long-term spectral stability by forming heterostructures. Silver is a promising plasmonic component with the lowest optical loss, but it suffers from dramatic damping of optical properties after surface oxidation, which limits its range of use and practical applications. Remarkably, the cSMAPs showed very high chemical and spectral stabilities over a long period of time; the Ag part is not oxidized in water and is not selectively etched, even by strong Ag-etching reagents [Figures 3k,l and S4 (SI)]. As shown in Figure 3k, with a similar Ag size of 20 nm, the SERS intensity of cSMAP38 is about 1.4 times higher than that of 20 nm AgNPs (AgNP20), which can be attributed to the structure-dependent electromagnetic field enhancement (Figure S5, SI). Moreover, the SERS intensity of AgNP20 dramatically decreased after a few days, and the SERS activity was lost within 15 days, while cSMAP38 maintained over 95% of its SERS signal intensity, even after 90 days (Figure 3l). In hetero-NPs, the dissolution of the Ag part is in equilibrium with the dissolution of the Ag_2S part and the heterointerface, and this is responsible for their higher stability toward oxidation.

The strain-releasing tendency in nanocrystals is based on the reduction of their Gibbs free energy, which can be expressed as the sum of surface/interface energy[23] and bulk energy (the cohesive interactions within a NP).[24] Thiolate ligands have a strong binding affinity to both Ag and Ag_2S surfaces that can
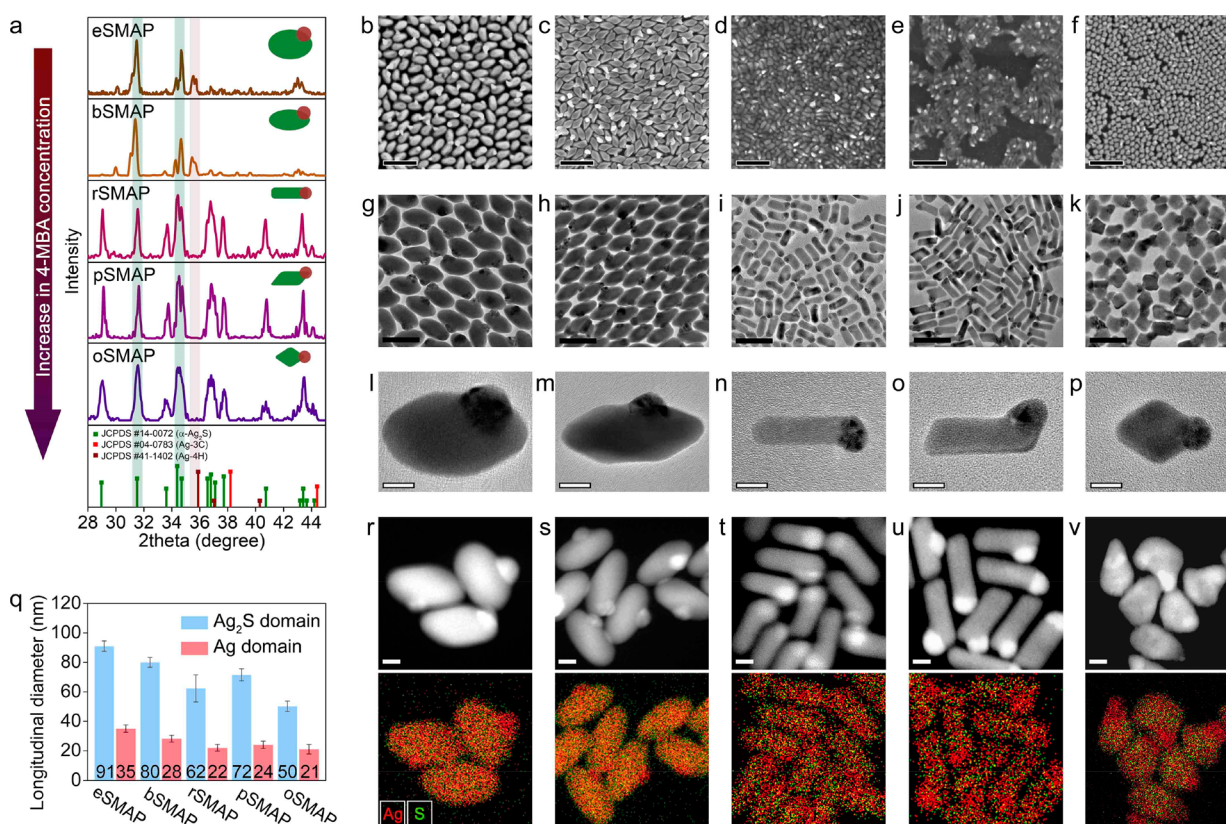
Figure 4. Ligand-induced shape engineering. (a) XRS patterns of various structure-engineered SMAPs, which are referred to according to the shapes of the Ag_2S domain, including ellipsoid (eSMAPs), bipyramid (bSMAPs), rod (rSMAPs), parallelepiped (pSMAPs), and octahedron (oSMAPs). SEM images (b−f), low-magnification TEM images (g−k), high-magnification TEM images (l−p), and HAADF images (r−v) and corresponding EDX elemental mapping results of eSMAPs, bSMAPs, rSMAPs, pSMAPs, and oSMAPs. (q) Statistical analysis of domain diameters in various structure-engineered SMAPs. Scale bars are 200 nm (b−f), 100 nm (g−k), 20 nm (l−p, r−v).

continuously modulate the surface/interface energies by simply tuning their concentrations.[25,26] Thus, we developed a surface-ligand-based designing principle for hetero-NPs by introducing a thiolate ligand [4-mercaptobenzoic acid (4-MBA)] into the 1HIM process to allow the dynamic tuning of surface/interface energies on the growing hetero-NPs (Figure 4a). As the 4-MBA concentration increased, the heterostructures continuously evolved from the shape of an ellipsoid (eSMAPs) to bipyramid (bSMAPs), rod (rSMAPs), parallelepiped (pSMAPs), and octahedron (oSMAPs) shapes, as shown by SEM (Figure 4b−f) and TEM (Figure 4g−p). The synthetic yield for each structure was estimated to be around 98% (eSMAPs), 95% (bSMAPs), 88% (rSMAPs), 92% (pSMAPs), and 99% (oSMAPs) (>500 nanoparticles were analyzed in each case). Particle diameters for each structure are summarized in Figure 4q, and the elemental distributions of silver and sulfur in each structure are analyzed by EDX mapping (Figure 4r−v). Importantly, the XRS patterns evolve with the geometric tuning of the heterostructures (Figure 4a), indicating the continuous adjustment of the crystal structure while tuning the surface ligand concentration.

When the 4-MBA concentration is relatively low (Figure 4a, eSMAPs and bSMAPs), the XRS patterns are similar to those of cSMAPs (Figure 3j), while it should be noted that the ratio of ($\bar{1}12$) intensity to (022) intensity increased. A further increase of 4-MBA concentration (Figure 4a, rSMAPs, pSMAPs, and oSMAPs) led to major changes in the XRS patterns with regard to the number and intensity of peaks, and these match well with that of bulk α-Ag_2S (PDF #14-0072).

Interestingly, the 4H-Ag peak at 35.7° disappears in the patterns of rSMAPs, pSMAPs, and oSMAPs, and this suggests that a lower surface energy of the growing NPs at a high 4-MBA concentration decreases the thermodynamic tendency for strain release and does not induce a major phase transition in either Ag_2S or Ag parts. The mechanism behind this unprecedented structural/crystalline controllability with the 1HIM may open a new avenue for the designing, synthesis, and subparticle-engineering of heterointerfacial nanostructures, particularly at room temperature.

Next, the Ag/Ag_2S heterostructures were converted into their Au/Ag_2S or Pt/Ag_2S counterparts by an anisotropic galvanic replacement reaction to investigate the role of multiple metal/Ag_2S heterointerfaces in forming heterostructured nanoframes (Figure S6, SI). Au was selectively deposited onto the Ag domain to maintain a Janus SMAP structure while the Pt was preferentially deposited onto the Ag_2S domain surface to form a $Ag/Ag_2S/Pt$ structure. The fact that the Ag domain cannot be fully replaced by excess Pt precursors at room temperature hints at the existence of a thermodynamic barrier for the further oxidative dissolution of Ag by the galvanic replacement reaction. We then performed the Pt replacement reaction at 95 °C (Figure S7, SI). Interestingly, the structure went through a strain-release-driven self-etching process to produce a single-crystalline hollow NP.

Single-crystalline hollow nanostructures, represented by nanoframes[27−29] and nanocages,[30−33] are of particular importance in catalysis,[27−30] optics,[32] and biomedical applications,[33] due to their tunable exquisite three-dimensional
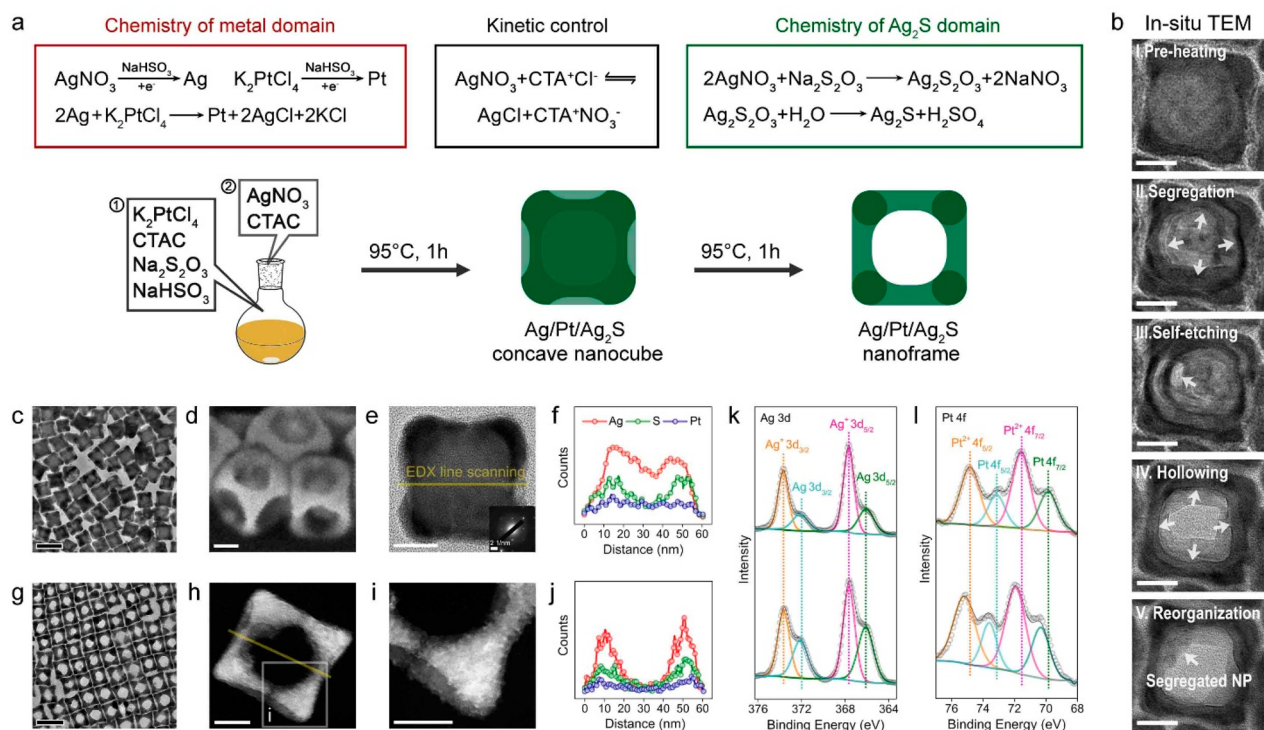
Figure 5. Heterointerface-induced structure evolution. (a) Schematic illustration of the 1HIM chemistry with bimetal/semiconductor heterointerfaces to form heterostructured nanocube frames. (b) In situ heating TEM measurements showing the transformation from the intermediate concave nanocubes to nanoframes. Large-scale TEM image (c), SEM image (d), single-particle HRTEM image (e), and corresponding EDX line scanning profile (f) of the intermediate concave nanocube structure. The inset of panel e shows the electron diffraction pattern of the particle. Large-scale TEM image (g), single-particle HAADF image (h), region-magnified HAADF image (i), and corresponding EDX line scanning profile (j) of the resulting nanoframe (MSF) structure. High-resolution X-ray photoelectron spectroscopy (XPS) spectra of a concave nanocube structure (first row) and nanoframe structure (second row) in terms of Ag 3d (k) and Pt 4f (l). Scale bars are 100 nm (c, g) and 20 nm (b, d, e, h, i).

structure, highly porous nature, large surface area, and novel physicochemical properties. Despite the relatively well-studied metal nanoframes,[27−29] the synthetic methodology and property of heterostructured nanoframes, especially for metal/semiconductor nanoframes with great potential in quantum confinement and electronic enhancement, have not been systematically established. As shown in Figure 5a, a well-defined cubic nanoframe structure can be obtained through an intermediate concave nanocube structure by introducing Pt(II) precursors into the 1HIM reaction. In situ TEM images (Figure 5b) revealed that the Ag/Pt/Ag$_2$S concave nanocube structure has gone through several stages to form a cubic Ag/Pt/Ag$_2$S nanoframe (metal−semiconductor nanoframe, MSF) structure, from segregation to self-etching, hollowing, and reorganization. As shown in Figure 5b, a higher-contrast phase started to segregate outward from the nanocube center, followed by self-etching and hollowing to form a cubic nanoframe, which was then reorganized to form relatively smooth inner edge surfaces with segregated NPs of the higher-contrast phase. To investigate the mechanism, these two structures were characterized by electron microscopy, EDX measurement, and XPS [Figures 5c−l and S8 (SI)]. According to the EDX data, the distribution of S was less affected by the frame-forming process, while those of Pt and Ag were localized to the outer edges of the nanoframe (Figure 5f,j). From the XPS spectra, the relative ratio of Ag$^+$ to Ag should be attributed to the etching of the Ag$_2$S domains (Figure 5k). For Pt 4f, the relative ratio of Pt^{2+} to Pt decreased about 21.3% after the frame-forming process (Figure 5l), indicating an

increase in the metallic state. The binding energies in the Pt 4f spectra increased about 0.5 eV after forming the nanoframes, which is often associated with the evolutions in the local chemical environment, further supporting the segregation of the Pt elements during the frame-forming process. Moreover, the existence of Ag, S, and Pt in MSFs was also evidenced by EDX spectrum, EDX mapping, and XRS patterns (Figure S8, SI). Compared to metal nanoframes,[27,34,35] semiconductor nanoframes are much less studied due to the difficulty in precise crystalline-engineering in a high yield. As shown in Figure 6, the primary and secondary MSF structures (Figure 6a) were found to be highly tunable (Figure 6b) by controlling precursor concentration ratios. As the [K$_2$PtCl$_4$]/[Na$_2$S$_2$O$_3$] increased, the shape of the MSF first changed from a polyhedral MSF (MSF I, Figure 6c−f) to a thick-framed cubic MSF (MSF II, Figure 6g−j), and then the edge-to-body diameter ratio of the nanoframes gradually decreased to form a cubic MSF (MSF III, Figure 6k−n) and a thin-framed cubic MSF (MSF IV, Figure 6o−r). Remarkably, the synthetic yields for these structures are around 88%, 92%, 90% and 85% for MSF I, MSF II, MSF III, and MSF IV, respectively (>500 nanoparticles were analyzed in each case).

Band gap engineering is a key process for the design and use of semiconductor materials and devices.[36,37] Due to quantum confinement, the band gap of semiconductors increases with their decreasing diameters.[38] Besides diameter control,[37] electronic impurity doping,[39] tuning of lattice structure (e.g., phase and defect engineering[37]), and external intervention (e.g., electric field[40]) can be also ways of tuning the
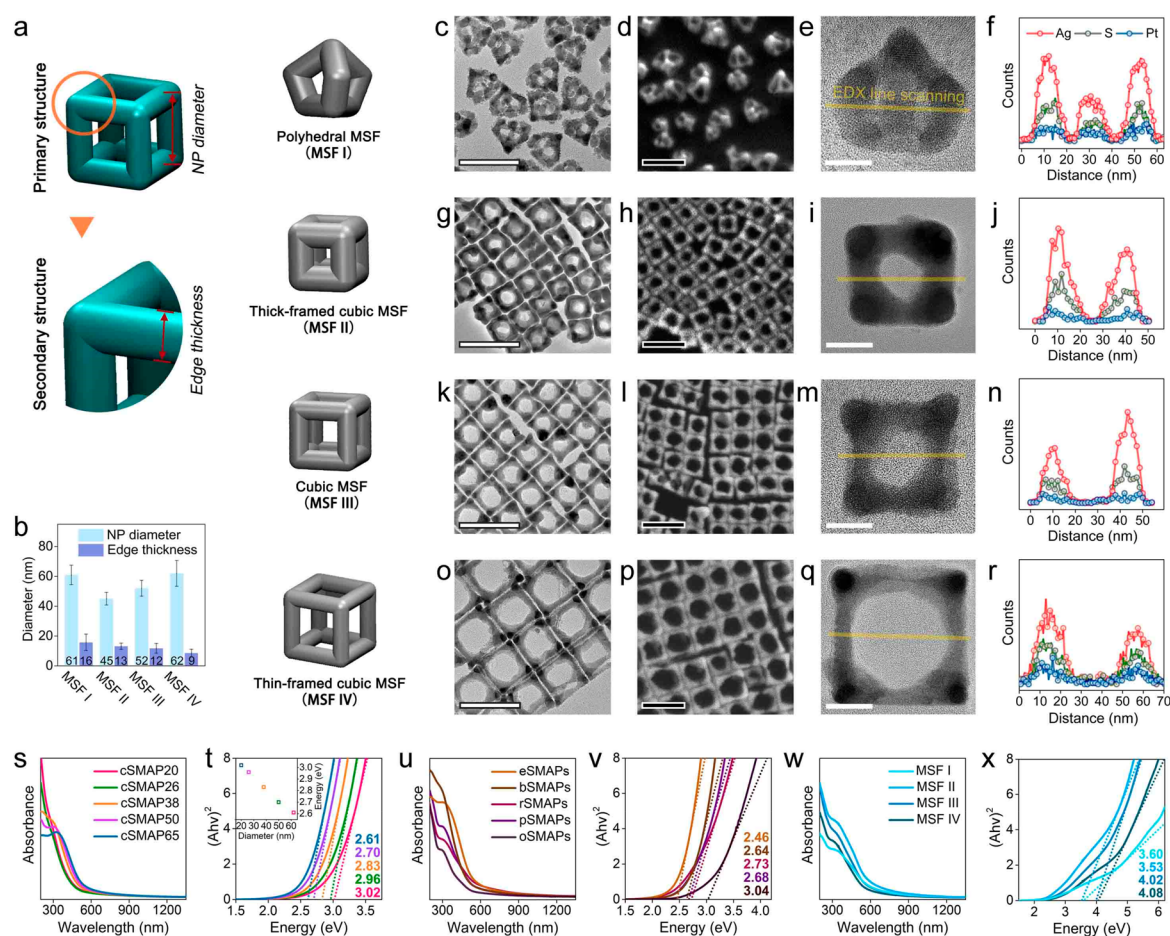
Figure 6. Secondary structural engineering and optical tuning. (a) Schematic illustration of the primary and secondary structural engineering of MSF and various structure-engineered MSFs. (b) Statistical analysis of structure diameters in various structure-engineered MSFs. TEM images (c, g, k, o), SEM images (d, h, l, p), single-particle HRTEM images (e, i, m, q), and corresponding EDX line scanning profile (f, j, n, r) of various structure-engineered MSFs (from top to bottom, MSF I to MSF IV). UV−vis−NIR spectra and the corresponding calculated optical band gaps of various size-controlled cSMAPs (s, t), various shape-engineered SMAPs (u, v), and various structure-engineered MSFs (w, x), estimated by Tauc plots. Scale bars are 100 nm (c, d, g, h, k, l, o, p) and 20 nm (e, i, m, q).

semiconductor band gap. Since the unique, diverse crystalline engineering, geometry control, and heterointerfacial tuning are possible with the 1HIM method, it is worthwhile to explore the band gap engineering capability of the 1HIM-generated hetero-NPs. First, it was shown that the optical properties of these heterostructures can be controlled by changing the diameter (Figure 6s,t), geometry (Figure 6u,v), and secondary structure (Figure 6w,x). As shown in Figure 6t, as the diameter of the cSMAPs decreases from 65 to 20 nm (Figure 3i), the optical band gap, estimated from Tauc plots,[41−43] gradually increased from 2.61 to 3.02 eV. Interestingly, as the shape of the SMAPs is altered by a change in surface ligand concentration, the band gap was clearly affected by the geometric changes (from 2.46 to 3.04 eV; Figure 6v). Particularly, for highly anisotropic bSMAPs, rSMAPs, and pSMAPs, the band gap change was not dominated by particle diameter but mainly influenced by particle shape. It should be noted that these trends and structures offer a wide range of band gap engineering capability and better understanding on how the structure, composition, and heterointerface affect the band gap and other related properties of hetero-NPs.[39,44] It was also found that the engineering of the frame thickness in a MSF affects the band gap values (Figure 6b), introducing another way of engineering the band gap from 3.53 to 4.08 eV,

which covers a different range of band gap energies (Figure 6x).

4. CONCLUSION

In summary, we developed and explored the 1HIM method as a generally applicable one-pot synthetic strategy to form a wide range of different heterostructured nanoparticles in a facile manner. Significantly, dynamic interface evolution between different components inside a particle has been observed with multiple equilibrium stages using the 1HIM strategy, in which single-crystalline semiconductor sub-NPs can be formed in a high yield. It was also shown that these hetero-NPs can offer improved, synergistic, or newly emerging properties and functions, particularly with intraparticle interfacial structure controllability, that cannot be obtained with single-component systems. As proof-of-concept experiments, we synthesized a series of anisotropic metal−semiconductor hetero-NPs, including heteronanoframes, at a relatively low temperature (<100 °C), and the formed structures can be highly tunable with respect to geometry, intraparticle interface, and properties, as well as structural and compositional details. Interestingly, the synergistic properties between interfacing components (semiconductor and metal) inside a particle were observed to have very high chemical and SERS spectral

Journal of the American Chemical Society
pubs.acs.org/JACS
Article

stabilities over a long period of time for cSMAPs and precise band gap engineering capability with SMAPs and MSFs. The fundamental understanding of growth behavior and mechanisms in heterostructures and controlling the heterointerfaces inside a hetero-NP have been the key hurdles in overcoming the current limitations for the high-yield synthesis of widely different hetero-NPs with high structural precision and crystallinity. The 1HIM method can address these issues, and the method and underlying logic that we have presented here offer new perspectives for a rational design and a powerful tool in the synthesis of a variety of different hetero-NPs, including previously unobtainable semiconductor−metal nanoframe structures. The 1HIM method can be readily applied to the synthesis of many combinations of different components in forming hetero-NPs, and more exquisite and complex heteronanostructures with unexplored functions and properties that cannot be synthesized with widely used SHN methods can be obtained using 1HIM in a facile manner.

■ ASSOCIATED CONTENT

Ⓢ Supporting Information

The Supporting Information is available free of charge at https://pubs.acs.org/doi/10.1021/jacs.0c11557.

> Complete experimental details and Figures S1−S8, showing additional characterization data (PDF)

■ AUTHOR INFORMATION

Corresponding Author

Jwa-Min Nam − Department of Chemistry, Seoul National University, Gwanak-gu, Seoul 08826, Korea; ⓞ orcid.org/0000-0002-7891-8482; Email: jmnam@snu.ac.kr

Authors

Mouhong Lin − Department of Chemistry, Seoul National University, Gwanak-gu, Seoul 08826, Korea

Jian Wang − Department of Chemistry, Seoul National University, Gwanak-gu, Seoul 08826, Korea; ⓞ orcid.org/0000-0002-6800-0467

Gyeong-Hwan Kim − Department of Chemistry, Seoul National University, Gwanak-gu, Seoul 08826, Korea

Jianan Liu − School of Chemical and Biological Engineering, Institute of Chemical Process, Seoul National University, Gwanak-gu, Seoul 08826, Korea; Center for Nanoparticle Research, Institute for Basic Science, Seoul 08826, Korea

Limin Pan − Department of Chemistry, Seoul National University, Gwanak-gu, Seoul 08826, Korea; School of Chemical and Biological Engineering, Institute of Chemical Process, Seoul National University, Gwanak-gu, Seoul 08826, Korea; Center for Nanoparticle Research, Institute for Basic Science, Seoul 08826, Korea

Yeonhee Lee − Department of Chemistry, Seoul National University, Gwanak-gu, Seoul 08826, Korea

Jeong-Wook Oh − Department of Chemistry, Seoul National University, Gwanak-gu, Seoul 08826, Korea

Yoonjae Jung − Department of Chemistry, Seoul National University, Gwanak-gu, Seoul 08826, Korea

Sungjae Seo − Department of Chemistry, Seoul National University, Gwanak-gu, Seoul 08826, Korea

Youngju Son − School of Chemical and Biological Engineering, Institute of Chemical Process, Seoul National University, Gwanak-gu, Seoul 08826, Korea; Center for Nanoparticle Research, Institute for Basic Science, Seoul 08826, Korea

Jongwoo Lim − Department of Chemistry, Seoul National University, Gwanak-gu, Seoul 08826, Korea

Jungwon Park − School of Chemical and Biological Engineering, Institute of Chemical Process, Seoul National University, Gwanak-gu, Seoul 08826, Korea; Center for Nanoparticle Research, Institute for Basic Science, Seoul 08826, Korea; ⓞ orcid.org/0000-0003-2927-4331

Taeghwan Hyeon − School of Chemical and Biological Engineering, Institute of Chemical Process, Seoul National University, Gwanak-gu, Seoul 08826, Korea; Center for Nanoparticle Research, Institute for Basic Science, Seoul 08826, Korea; ⓞ orcid.org/0000-0001-5959-6257

Complete contact information is available at:
https://pubs.acs.org/10.1021/jacs.0c11557

Author Contributions

‖M.L., J.W., and G.-H.K. contributed equally to this work.

Notes

The authors declare no competing financial interest.

■ ACKNOWLEDGMENTS

■ REFERENCES

(1) Tan, C.; Chen, J.; Wu, X.-J.; Zhang, H. Epitaxial Growth of Hybrid Nanostructures. Nat. Rev. Mater. 2018, 3 (2), 17089.

(2) Ha, M.; Kim, J.-H.; You, M.; Li, Q.; Fan, C.; Nam, J.-M. Multicomponent Plasmonic Nanoparticles: From Heterostructured Nanoparticles to Colloidal Composite Nanostructures. Chem. Rev. 2019, 119 (24), 12208−12278.

(3) Kim, S.; Kim, J.-M.; Park, J.-E.; Nam, J.-M. Nonnoble-Metal-Based Plasmonic Nanomaterials: Recent Advances and Future Perspectives. Adv. Mater. 2018, 30 (42), 1704528.

(4) Mishra, U. Semiconductor Device Physics and Design; Springer: Dordrecht, 2014.

(5) Diao, Y.; Tee, B. C. K.; Giri, G.; Xu, J.; Kim, D. H.; Becerril, H. A.; Stoltenberg, R. M.; Lee, T. H.; Xue, G.; Mannsfeld, S. C. B.; Bao, Z. Solution Coating of Large-Area Organic Semiconductor Thin Films with Aligned Single-Crystalline Domains. Nat. Mater. 2013, 12, 665−671.

(6) Morales, A. M.; Lieber, C. M. A Laser Ablation Method for the Synthesis of Crystalline Semiconductor Nanowires. Science 1998, 279 (5348), 208−211.

(7) Zhang, J.; Tang, Y.; Lee, K.; Ouyang, M. Nonepitaxial Growth of Hybrid Core-Shell Nanostructures with Large Lattice Mismatches. Science 2010, 327 (5973), 1634−1638.

(8) Wu, K.; Chen, J.; McBride, J. R.; Lian, T. Efficient Hot-Electron Transfer by a Plasmon-Induced Interfacial Charge-Transfer Transition. Science 2015, 349 (6248), 632−635.

(9) Wu, B. H.; Liu, D. Y.; Mubeen, S.; Chuong, T. T.; Moskovits, M.; Stucky, G. D. Anisotropic Growth of Tio2 onto Gold Nanorods for Plasmon-Enhanced Hydrogen Production from Water Reduction. J. Am. Chem. Soc. 2016, 138 (4), 1114−1117.

(10) Kim, S.; Fisher, B.; Eisler, H.-J.; Bawendi, M. Type-Ii Quantum Dots: Cdte/Cdse(Core/Shell) and Cdse/Znte(Core/Shell) Heterostructures. J. Am. Chem. Soc. 2003, 125 (38), 11466−11467.

(11) Kawawaki, T.; Nakagawa, T.; Sakamoto, M.; Teranishi, T. Carrier-Selective Blocking Layer Synergistically Improves the Plasmonic Enhancement Effect. J. Am. Chem. Soc. 2019, 141 (21), 8402−8406.

(12) Xu, W.; Liu, W.; Schmidt, J. F.; Zhao, W.; Lu, X.; Raab, T.; Diederichs, C.; Gao, W.; Seletskiy, D. V.; Xiong, Q. Correlated Fluorescence Blinking in Two-Dimensional Semiconductor Heterostructures. *Nature* **2017**, *541*, 62−67.

(13) Habas, S. E.; Lee, H.; Radmilovic, V.; Somorjai, G. A.; Yang, P. Shaping Binary Metal Nanocrystals through Epitaxial Seeded Growth. *Nat. Mater.* **2007**, *6*, 692−697.

(14) Lin, M.; Kim, G.-H.; Kim, J.-H.; Oh, J.-W.; Nam, J.-M. Transformative Heterointerface Evolution and Plasmonic Tuning of Anisotropic Trimetallic Nanoparticles. *J. Am. Chem. Soc.* **2017**, *139* (30), 10180−10183.

(15) Buck, M. R.; Bondi, J. F.; Schaak, R. E. A Total-Synthesis Framework for the Construction of High-Order Colloidal Hybrid Nanoparticles. *Nat. Chem.* **2012**, *4* (1), 37−44.

(16) Fenton, J. L.; Steimle, B. C.; Schaak, R. E. Tunable Intraparticle Frameworks for Creating Complex Heterostructured Nanoparticle Libraries. *Science* **2018**, *360* (6388), 513−517.

(17) Liu, X.; Zhang, F.; Jing, X.; Pan, M.; Liu, P.; Li, W.; Zhu, B.; Li, J.; Chen, H.; Wang, L.; Lin, J.; Liu, Y.; Zhao, D.; Yan, H.; Fan, C. Complex Silica Composite Nanomaterials Templated with DNA Origami. *Nature* **2018**, *559* (7715), 593−598.

(18) Kwon, S. G.; Krylova, G.; Phillips, P. J.; Klie, R. F.; Chattopadhyay, S.; Shibata, T.; Bunel, E. E.; Liu, Y. Z.; Prakapenka, V. B.; Lee, B.; Shevchenko, E. V. Heterogeneous Nucleation and Shape Transformation of Multicomponent Metallic Nanostructures. *Nat. Mater.* **2015**, *14* (2), 215−223.

(19) Xia, Y. N.; Xia, X. H.; Peng, H. C. Shape-Controlled Synthesis of Colloidal Metal Nanocrystals: Thermodynamic Versus Kinetic Products. *J. Am. Chem. Soc.* **2015**, *137* (25), 7947−7966.

(20) Wang, Y. W.; He, J. T.; Liu, C. C.; Chong, W. H.; Chen, H. Y. Thermodynamics Versus Kinetics in Nanosynthesis. *Angew. Chem., Int. Ed.* **2015**, *54* (7), 2022−2051.

(21) Chen, Y.; Lai, Z.; Zhang, X.; Fan, Z.; He, Q.; Tan, C.; Zhang, H. Phase Engineering of Nanomaterials. *Nat. Rev. Chem.* **2020**, *4* (5), 243−256.

(22) Vitos, L.; Ruban, A. V.; Skriver, H. L.; Kollár, J. The Surface Energy of Metals. *Surf. Sci.* **1998**, *411* (1), 186−202.

(23) Wang, Y.; He, J.; Liu, C.; Chong, W. H.; Chen, H. Thermodynamics Versus Kinetics in Nanosynthesis. *Angew. Chem., Int. Ed.* **2015**, *54* (7), 2022−2051.

(24) Barnard, A. S.; Zapol, P. A Model for the Phase Stability of Arbitrary Nanoparticles as a Function of Size and Shape. *J. Chem. Phys.* **2004**, *121* (9), 4276−4283.

(25) Feng, Y. H.; He, J. T.; Wang, H.; Tay, Y. Y.; Sun, H.; Zhu, L. F.; Chen, H. Y. An Unconventional Role of Ligand in Continuously Tuning of Metal-Metal Interfacial Strain. *J. Am. Chem. Soc.* **2012**, *134* (4), 2004−2007.

(26) Wang, Z. X.; He, B. W.; Xu, G. F.; Wang, G. J.; Wang, J. Y.; Feng, Y. H.; Su, D. M.; Chen, B.; Li, H.; Wu, Z. H.; Zhang, H.; Shao, L.; Chen, H. Y. Transformable Masks for Colloidal Nanosynthesis. *Nat. Commun.* **2018**, *9* (1), 563.

(27) Chen, C.; Kang, Y.; Huo, Z.; Zhu, Z.; Huang, W.; Xin, H. L.; Snyder, J. D.; Li, D.; Herron, J. A.; Mavrikakis, M.; Chi, M.; More, K. L.; Li, Y.; Markovic, N. M.; Somorjai, G. A.; Yang, P.; Stamenkovic, V. R. Highly Crystalline Multimetallic Nanoframes with Three-Dimensional Electrocatalytic Surfaces. *Science* **2014**, *343* (6177), 1339−1343.

(28) Niu, Z. Q.; Becknell, N.; Yu, Y.; Kim, D.; Chen, C.; Kornienko, N.; Somorjai, G. A.; Yang, P. D. Anisotropic Phase Segregation and Migration of Pt in Nanocrystals En Route to Nanoframe Catalysts. *Nat. Mater.* **2016**, *15* (11), 1188−1194.

(29) Wu, Y. E.; Wang, D. S.; Zhou, G.; Yu, R.; Chen, C.; Li, Y. D. Sophisticated Construction of Au Islands on Pt-Ni: An Ideal Trimetallic Nanoframe Catalyst. *J. Am. Chem. Soc.* **2014**, *136* (33), 11594−11597.

(30) Zhang, L.; Roling, L. T.; Wang, X.; Vara, M.; Chi, M.; Liu, J.; Choi, S. I.; Park, J.; Herron, J. A.; Xie, Z.; Mavrikakis, M.; Xia, Y. Platinum-Based Nanocages with Subnanometer-Thick Walls and Well-Defined, Controllable Facets. *Science* **2015**, *349* (6246), 412−416.

(31) Wu, H.-L.; Sato, R.; Yamaguchi, A.; Kimura, M.; Haruta, M.; Kurata, H.; Teranishi, T. Formation of Pseudomorphic Nanocages from Cu_2O Nanocrystals through Anion Exchange Reactions. *Science* **2016**, *351* (6279), 1306−1310.

(32) Chen, J.; Saeki, F.; Wiley, B. J.; Cang, H.; Cobb, M. J.; Li, Z. Y.; Au, L.; Zhang, H.; Kimmey, M. B.; Li, X. D.; Xia, Y. N. Gold Nanocages: Bioconjugation and Their Potential Use as Optical Imaging Contrast Agents. *Nano Lett.* **2005**, *5* (3), 473−477.

(33) Yavuz, M. S.; Cheng, Y.; Chen, J.; Cobley, C. M.; Zhang, Q.; Rycenga, M.; Xie, J.; Kim, C.; Song, K. H.; Schwartz, A. G.; Wang, L. V.; Xia, Y. Gold Nanocages Covered by Smart Polymers for Controlled Release with near-Infrared Light. *Nat. Mater.* **2009**, *8* (12), 935−939.

(34) Ham, S.; Jang, H. J.; Song, Y.; Shuford, K. L.; Park, S. Octahedral and Cubic Gold Nanoframes with Platinum Framework. *Angew. Chem., Int. Ed.* **2015**, *54* (31), 9025−9028.

(35) Hong, X.; Wang, D.; Cai, S.; Rong, H.; Li, Y. Single-Crystalline Octahedral Au-Ag Nanoframes. *J. Am. Chem. Soc.* **2012**, *134* (44), 18165−18168.

(36) Capasso, F. Band-Gap Engineering: From Physics and Materials to New Semiconductor Devices. *Science* **1987**, *235* (4785), 172−176.

(37) Ning, C.-Z.; Dou, L.; Yang, P. Bandgap Engineering in Semiconductor Alloy Nanomaterials with Widely Tunable Compositions. *Nat. Rev. Mater.* **2017**, *2* (12), 17070.

(38) Murray, C. B.; Norris, D. J.; Bawendi, M. G. Synthesis and Characterization of Nearly Monodisperse Cde (E = Sulfur, Selenium, Tellurium) Semiconductor Nanocrystallites. *J. Am. Chem. Soc.* **1993**, *115* (19), 8706−8715.

(39) Larquet, C.; Nguyen, A.-M.; Glais, E.; Paulatto, L.; Sassoye, C.; Selmane, M.; Lecante, P.; Maheu, C.; Geantet, C.; Cardenas, L.; Chanéac, C.; Gauzzi, A.; Sanchez, C.; Carenco, S. Band Gap Engineering from Cation Balance: The Case of Lanthanide Oxysulfide Nanoparticles. *Chem. Mater.* **2019**, *31* (14), 5014−5023.

(40) Oostinga, J. B.; Heersche, H. B.; Liu, X. L.; Morpurgo, A. F.; Vandersypen, L. M. K. Gate-Induced Insulating State in Bilayer Graphene Devices. *Nat. Mater.* **2008**, *7* (2), 151−157.

(41) Liao, W.-Q.; Zhang, Y.; Hu, C.-L.; Mao, J.-G.; Ye, H.-Y.; Li, P.-F.; Huang, S. D.; Xiong, R.-G. A Lead-Halide Perovskite Molecular Ferroelectric Semiconductor. *Nat. Commun.* **2015**, *6* (1), 7338.

(42) Saidaminov, M. I.; Abdelhady, A. L.; Murali, B.; Alarousu, E.; Burlakov, V. M.; Peng, W.; Dursun, I.; Wang, L.; He, Y.; Maculan, G.; Goriely, A.; Wu, T.; Mohammed, O. F.; Bakr, O. M. High-Quality Bulk Hybrid Perovskite Single Crystals within Minutes by Inverse Temperature Crystallization. *Nat. Commun.* **2015**, *6* (1), 7586.

(43) Xie, L.-Q.; Chen, L.; Nan, Z.-A.; Lin, H.-X.; Wang, T.; Zhan, D.-P.; Yan, J.-W.; Mao, B.-W.; Tian, Z.-Q. Understanding the Cubic Phase Stabilization and Crystallization Kinetics in Mixed Cations and Halides Perovskite Single Crystals. *J. Am. Chem. Soc.* **2017**, *139* (9), 3320−3323.

(44) Conley, H. J.; Wang, B.; Ziegler, J. I.; Haglund, R. F.; Pantelides, S. T.; Bolotin, K. I. Bandgap Engineering of Strained Monolayer and Bilayer MoS_2. *Nano Lett.* **2013**, *13* (8), 3626−3630.